

# Bond angle distribution in amorphous germania and silica

Jörg Neuefeind

Hamburger Synchrotronstrahlungslabor HASYLAB at Deutsches Elektronensynchrotron DESY,  
Notkestrasse 85, 22603 Hamburg, Germany

K. -D. Liss

European Synchrotron Radiation Facility ESRF, B. P. 220, 38043 Grenoble, France

## Abstract

The distribution of Ge-O-Ge and Si-O-Si bond angles  $\alpha$  in amorphous germania and silica is re-determined on the basis of diffraction experiments. The bond angle  $\alpha$  joining adjacent tetrahedra is the central parameter of any continuous random network description (CRN) of these glasses. New high energy photon diffraction experiments on amorphous germania (at photon energies of 97 and 149 keV) are presented, covering the momentum transfer  $0.6\text{-}33.5\text{\AA}^{-1}$ . In photon diffraction experiments on  $\text{GeO}_2$  the contribution of the OO pairs is very small. To obtain a similar information for amorphous  $\text{SiO}_2$ , high energy photon diffraction experiments [1] have been combined with neutron diffraction data [2, 3] on amorphous silica in order to eliminate the OO-partial structure factor. With this technique it is shown that the Si-O-Si angle distribution is fairly narrow ( $\sigma = 7.5^\circ$ ) and in fact comparable in width to the Ge-O-Ge angle distribution ( $\sigma = 8.3^\circ$ ), a result which differs from current opinion. The narrower distribution found in this study are in much better agreement to the determinations based on  $^{29}\text{Si}$ -MAS-NMR. Among the various models relating the chemical shift to the bond angle, best agreement is found with those models based on the secant model. Sharp components in the bond angle distribution can be excluded within the reached real space resolution of  $0.09\text{\AA}$ .

## 1 Introduction

Vitreous silica and germania are two prototype simple glasses. These two glasses consist of corner-sharing tetrahedra linked to a continuous three-dimensional network. Numerous diffraction experiments have been published, especially concerning amorphous silica, of which the eldest date back to the very beginning of x-ray diffraction [4]. But even before, some ideas about the structure of glass already existed [5]. The traditional theories of glass structure are the crystallite theory and the continuous random network (CRN) theory attributed to Lebedev [6] and Zachariasen [7] respectively. Modern crystallite theory predicts fluctuations of the intermediate range order where some regions approach the atomic arrangement of the crystal. Fluctuations of the intermediate range order are also allowed in the CRN model, so the difference between both models is mainly a gradual one. As bond angles in crystals show only small variations around discrete values, modern crystallite theory should lead to sharp bond angle distributions superimposed on the broader distribution prevailing in the more disordered interconnecting regions. A more detailed discussion of these topics is given in the review articles of Wright [8] and Porai-Koshits [9].

The central parameter of a CRN model of germania and silica is the distribution of A-O-A bond angles (A=Si,Ge) joining adjacent tetrahedra. The Si-O-Si angle distribution in amorphous  $\text{SiO}_2$  is often believed to be much broader than the corresponding distribution in germania. This can be traced back to the classical work of Mozzi and Warren [10]. Later

some discussion came up about the average Si-O-Si angle [11, 12], but not about the width of the distribution. As the mean Ge-O-Ge angle of  $133^\circ$  is close to the one for planar 3-membered rings, Barrio *et al.* [13] recently argued, that the narrower distribution in  $\text{GeO}_2$  is an indication for the presence of such small, stiff ring-systems in a much larger extent than in  $\text{SiO}_2$ . This hypothesis was inspired by the interpretation of IR-data of these glasses. Robertson *et al.* [14] computer relaxed the Bell and Dean [15] CRN model, but were quite suspicious on their result, as the Si-O-Si angle distribution found was much narrower than the Mozzi and Warren distribution.

The Si-O-Si angle can also be determined with  $^{29}\text{Si}$ -MAS-NMR spectroscopy. The method is based on the assumption that a functional relation exists between the chemical shift  $\delta_{NMR}$  and the Si-O-Si bond angle. This relation has to be established experimentally in measuring the chemical shifts of a sufficiently large number of crystalline  $\text{SiO}_2$  polymorphs with known Si-O-Si bond angles. The first Si-O-Si angle determination by this technique was described by Dupree and Pettifer [16]. This first distribution was claimed to be very broad (FWHM  $40^\circ$  !) and essentially flat between  $140$ - $155^\circ$ . This result was later on revised, being attributed to boron, sodium and aluminum contaminants present in the investigated glass sample [17]. In this paper also the influence of various assumptions on the relation between the chemical shift and the bond angle is discussed. In general, the bond angle distributions determined with NMR are found to be substantially narrower [17, 18] than the Mozzi and Warren distribution, although in [18] a good agreement with Mozzi and Warrens result is claimed (This is certainly to be understood in comparison to [16]). MD simulation sometimes agree with the NMR results [19], while other recent simulations [20] find good agreement with Mozzi and Warrens result and a third group reported even a broader distribution [21].

Recently, diffraction experiments on amorphous systems (glasses: [1], molecular liquids: [22]) with high energy photons as delivered from modern synchrotron radiation sources became feasible. The term high energy photons will be used for photons in the energy range of  $\sim 80 - 200$  keV, i.e. of an energy about one order of magnitude higher than that of x-rays traditionally used in angle dispersive measurements. As the photo-electrical absorption decreases with energy approximately like  $E^3$ , the absorption is reduced by three orders of magnitude. Scattering therefore becomes the dominant process in a large number of materials and the conditions of the experiment become in general quite similar to that of a typical neutron diffraction experiment. The wavelength of the photons is quite short and consequently no principle limit exist on the maximum momentum transfer attainable: The momentum transfer for back scattering with a photon energy of 100 keV is  $Q_{max} = 4\pi E/(hc) = 4\pi E \cdot 0.080658\text{keV}^{-1}\text{\AA}^{-1} = 101.4\text{\AA}^{-1}$ . Considering only a more commonly used momentum transfer range the scattering takes place through small or intermediate scattering angles. This is advantageous for the use of small windows or flat area detectors, but the first two characteristics - low absorption and high momentum transfer - will be more important for the present study. For a description of the use of high energy photons in general - i. e. not restricted to amorphous substances - see [23].

This article will focus on the Si-O-Si and the Ge-O-Ge bond angle distributions and its comparison. The data on amorphous germania are new and the experiment is described in the following section. The experiment on vitreous silica at the DORIS-III synchrotron has been described previously [1]. The neutron diffraction data on amorphous silica have been taken from [2] and [3].

## 2 Experiment on germania

The vitreous germania has been prepared from 99.999% pure  $\text{GeO}_2$  (Strem-Chemicals, Newburyport, MA, USA) by melting the crystalline material. The melt was kept for 8 h at 1473 K at atmospheric pressure (melting point 1383 K). The furnace was then switched off and the sample cooled to 900 K in about 10 min. The resulting sample was clouded as a result of the inclusion of small gas bubbles but no traces of crystallinity were left.

The diffraction experiment on vitreous germania has been carried out at the high energy beam-line ID15A of the European Synchrotron Radiation Facility ESRF. The Synchrotron was operated in 16 bunch mode with an average current of about 70 mA and beam lifetimes of about 16 h. The beam-line is designed to operate alternatively with a permanent magnet multipole wiggler or with a super conducting wavelength shifter [24]. The former only is commissioned at the moment and thus has been used for the experiment. Its gap was maximal closed to 20.3 mm leading to a critical energy of 43 keV. To remove the heat load, lower energies are cut by a cooled 4 mm aluminum filter. The beam size can be chosen by a set of water-cooled secondary slits in front of the monochromator position in the optics hutch II [24].

A perfect (220) Si crystal in Laue geometry was used for monochromatization and mounted on a bending device. To reduce background in the experimental hutch, the white beam was stopped in the optics hutch II.

A dedicated two axes diffractometer at the high energy beam-line does not exist. Instead the sample was mounted on the analyzer stage of the triple axes diffractometer. Here, the scattering angle is chosen by a translation of the detector perpendicular to the white beam axis. This geometry allows to select a maximum scattering angle of  $2\theta = 26^\circ$ . The solid state detector was equipped with a 30 mm thick germanium crystal and has a typical energy resolution of about 1 keV. Discriminating the energy around the photon energy of the monochromatic beam reduces the background scattered from the white beam. The intensity in the first sharp diffraction peak of the sample was around  $5 \cdot 10^4$  counts per second. Further increase of the intensity would raise considerable dead-time problems. In order to cover a large momentum transfer range two different photon energies of 97.58 keV and 149.80 keV were chosen. The monochromator was bent for the higher energy setup in order to compensate for the intensity drop.

The energy of the primary beam was determined by observing the Bragg peak position of a second perfect (220) Si crystal mounted on the monochromator position of the triple-axes diffractometer for both, dispersive and non-dispersive geometry.

Due to the excellent beam stability of the ESRF synchrotron, normalizing the data on the beam current was found to be more convenient than using an NaI monitor, which was installed for control purposes. The latter observes the air scattering produced by the incoming beam and was too sensitive to the hutch background as its energy resolution is too poor. The problems associated with beam fluctuations described in [1] are mostly reduced in the present study. In order to minimize generally the effect of drifts the data acquisition was organized as a sequence of several short scans.

The data were subsequently corrected for background, absorption, multiple scattering, polarization of the incoming beam, the variation of the solid angle seen by the detector as a result of the changing distance between the sample and the detector (tangential movement, see above) and the increased detection efficiency for inelastically scattered photons.  $\mu r$  is 0.25 at 149 keV (with  $\mu$  being the total absorption coefficient and  $r$  the radius of the sample). Air scattering is the dominant background contribution, especially at low Q's.

The correction procedure was described in detail in [1]. The resulting fully corrected and normalized data are presented in Fig. 1.

### 3 Data analysis

The usual definition of the structure functions in the neutron and photon case are:

$$S(Q) = \frac{\left(\frac{d\sigma}{d\Omega}\right)_{dist}^n}{\left(\sum_{uc} b_i\right)^2} = \sum_{jk} \frac{b_j b_k}{\left(\sum b_i\right)^2} s_{ij} \quad i(Q) = \frac{\left(\frac{d\sigma}{d\Omega}\right)_{dist}^x}{\left(\sum_{uc} f_i\right)^2} = \sum_{jk} \frac{f_j f_k}{\left(\sum f_i\right)^2} s_{ij} \quad (1)$$

where  $\left(\frac{d\sigma}{d\Omega}\right)_{dist}$  is the distinct (interference) differential cross section,  $S$  and  $b_i$  are the structure function and the scattering lengths in the neutron case,  $i$  and  $f_i$  are the structure function and the form-factors in the photon case, the sum is extending over the unit composition.  $S(Q)$  and  $i(Q)$  are weighted sums of the partial structure factors  $s_{jk}$ . The  $s_{jk}$  are, of course, the same in neutron and photon diffraction. The weighting coefficients in the photon case are constant in  $Q$  only if one assumes that the form factors of the atoms present differ by a scaling factor only - this is the K-approximation introduced by Warren, Krutter and Morningstar [25]. A combination of neutron and photon data given by:

$$d_{j'k'}(Q) = f_{j'} f_{k'} \left(\frac{d\sigma}{d\Omega}\right)_{dist}^n - b_{j'} b_{k'} \left(\frac{d\sigma}{d\Omega}\right)_{dist}^x = \sum_{jk \neq j'k'} (f_{j'} f_{k'} b_j b_k - b_{j'} b_{k'} f_j f_k) s_{jk} \quad (2)$$

eliminates one particular partial structure factor  $s_{j'k'}$  from the diffraction pattern without any approximation. This procedure is analogous to the isotope substitution technique in neutron diffraction, but has the advantage that the same sample can be used. Prerequisites for a successful separation are a good knowledge of the form-factors and of the neutron scattering lengths. The neutron scattering lengths used in the analysis are taken from [26], the form-factors from [27, 28].

The three differences which are possible for  $\text{SiO}_2$  according to Eq. (2) are shown in Fig. 2. The contribution of the first two peaks in real space - the SiO- and OO- first shell - calculated according to [3] is indicated. It is apparent from the figure that the scattering pattern is dominated by these peaks above  $15 \text{ \AA}^{-1}$ . It is also apparent that a systematic error is present between  $16 \text{ \AA}^{-1}$  and  $20 \text{ \AA}^{-1}$ , probably caused by the splicing of two scans in that region [1]. This can also be seen in Fig. 3 where the contribution of the first two peaks has been subtracted.

A useful real space correlation function which can be used for the analysis of amorphous materials is (in the neutron case):

$$T(r) = \frac{1}{2\pi^2 \rho} \int_{Q_{min}}^{Q_{max}} Q S(Q) M(Q) \sin(Qr) dQ + r = \sum_{jk} \frac{b_j b_k}{\left(\sum b\right)^2} t'_{jk}(r), \quad (3)$$

where  $M(Q)$  is an optional modification function.  $T(r)$  is related to  $g(r)$  - the correlation function which is more commonly used in the discussion of the structure of liquids - simply by  $T(r) = r g(r)$ . The experimental component correlation functions  $t'$  are related to the real component correlation functions  $t$  via a convolution with a peak shape function [10, 29]. The peak shape function is determined by the modification function used and - in photon diffraction - the non-constant weighting factors of the partial structure factors. The modification function used here is the rectangular function (all data points are equally

weighted for the Fourier transform):

$$M(Q) = \begin{cases} 0 & : Q < Q_{min} \\ 1 & : Q_{min} < Q < Q_{max} \\ 0 & : Q > Q_{max} \end{cases} \quad (4)$$

This is to the authors opinion a better solution than weighting parts of the measured data with a modification function as e. g. the one proposed by Lorch [30] as long as the implications on  $T(R)$  are noticed.

For the differences given by Eq. (2) the Fourier transform has been calculated according to:

$$T_{diff}(r) = \frac{1}{2\pi^2 \rho (f_{j'} f_{k'} b_{j''} b_{k''} - b_{j'} b_{k'} f_{j''} f_{k''}) N} \int_{Q_{min}}^{Q_{max}} Q d_{j'k'}(Q) M(Q) \sin(Qr) dQ + r \quad (5)$$

The division by  $f_{j'} f_{k'} b_{j''} b_{k''} - b_{j'} b_{k'} f_{j''} f_{k''}$  removes the dependence of the peak shape function from the non-constant weighting factors for one of the partial correlation functions (for  $j''k''$ ).  $N$  is defined by:

$$N = \sum_{jk \neq j'k'} \frac{f_{j'}(0) f_{k'}(0) b_j b_k - b_{j'} b_{k'} f_j(0) f_k(0)}{f_{j'}(0) f_{k'}(0) b_{j''} b_{k''} - b_{j'} b_{k'} f_{j''}(0) f_{k''}(0)} \quad (6)$$

Whenever comparisons between a model and the experiments are presented, a double Fourier-transform has been carried out: The model partial correlation functions  $t(r)$  are transformed into  $Q$ -space:

$$Qs(Q) = 4\pi\rho \int_0^\infty t(r) \sin(Qr) dr \quad (7)$$

multiplied by the appropriate weighting factors, summed and back transformed to  $r$ -space with the same  $Q$ -interval than the experimental data. In short, the model correlation functions are convolved with the appropriate peak shape function before comparison. The agreement with the experiment is judged according to [3] by calculating:

$$\chi^2 = \frac{1}{\int_{r_{min}}^{r_{max}} T_{exp}^2(r) dr} \int_{r_{min}}^{r_{max}} (T_{exp}(r) - T_{model})^2 dr \quad (8)$$

Models have been developed using a MC algorithm. The A-O bond length (with A=Si,Ge) is assumed to have a Gaussian form:

$$V(r_{A-O}) = K \cdot \exp \left[ -\frac{(r_{A-O} - r_0)^2}{2\sigma_r^2} \right], \quad (9)$$

with  $K$  being a scaling factor,  $r_{A-O}$  the bond length,  $r_0$  and  $\sigma_r$  having its usual significance. The bond angles A-O-A and O-A-O have been modeled by distributions of the form:

$$V(\alpha) = K \cdot \exp \left[ -\frac{(\alpha - \alpha_0)^2}{2\sigma^2} \right] \cdot \sin(\alpha), \quad (10)$$

with  $K$  again a scaling factor,  $\alpha$  the A-O-A bond angle,  $\alpha_0$  and  $\sigma$  are the free parameters of the distribution. The O-A-O bond angle will be called  $\beta$  in the following, and  $\alpha$  has to be replaced by  $\beta$  then in the above equation. The dihedral angle distribution has been given the form:

$$V(\delta) = K \cdot \sum_{i=1}^5 \exp \left[ -\frac{[\delta - \delta_0 \cdot (i-2)]^2}{2\sigma_\delta^2} \right], \quad (11)$$

where  $\delta$  is the dihedral angle A-O-A-O,  $\delta_0$  has been set to  $60^\circ$ ,  $K$  is a scaling factor and  $\sigma_\delta$  is a variable parameter. This leads to distributions having the necessary threefold symmetry favoring eclipsed conformation (In the limit  $\sigma_\delta \rightarrow \infty$  an uniform dihedral angle distribution is reached). Assuming independence of the above distributions the short to intermediate range order is specified: The A-O, O-O, A-A first and second shell contributions. These distributions are calculated and compared with the experiment via the above described formalism.

## 4 Simulation

To calculate the distance distributions from the distributions (9) -(11) chains O-A-O-A-O-A of A and O atoms were generated. Beginning the chain from one side - say with the O-atom a (normally distributed) random number determines the position of the next A-atom. The distribution (9) is, hence, fulfilled in this step. The position of the next O-atom is determined by two random numbers (representing distribution (9) and (10)), the following A-atom by three random numbers and so on. As only four-body correlations and no cross correlations are considered a maximum of three random numbers is needed for positioning an atom in the chain. Each chain yields five times a A-O first shell distance, two times a O-O and A-A first shell, three times a A-O second shell and one times a O-O and A-A second shell distance.  $10^5$  chains were generated for each model.

This MC approach has the advantage over the analytical approach followed in [1] to allow a much more flexible choice of distributions, while still being computationally very cheap (few seconds of CPU time). It has the disadvantage that the analytical form of the distributions has to be imposed in fore-hand. It is easy to overcome this problem, following the ideas of reverse Monte-Carlo (RMC) simulations [31]. First one generates chains with quite wide distributions of next neighbor distances, bond angles and dihedral angles. The generated chains are accepted or rejected using the Metropolis criterion, if these chains improve or deteriorate the agreement of the total model (the ensemble of chains accepted so far) with the experiment. This technique is by orders of magnitude more time consuming as it needs the double Fourier transforms described in the preceding chapter to be executed for each chain generated. The next more complex simulation would be a full RMC simulation of the system: This introduces an additional information into the simulation process, i. e. the macroscopic density, but on the other hand - a disadvantage in a system which is in reality of course aperiodic - periodic boundary conditions. A RMC simulation for  $\text{SiO}_2$  has already been carried out (including information from both neutron and photon diffraction experiments) [32] but it leads to structures which are apparently unphysical on various counts. One reason is perhaps, that a "good" structure can not be reached within the computer time available.

## 5 Results and Discussion

$T_x(r)$  for amorphous germania are shown in figure 4a. Looking closer at the GeO next neighbor peak in Fig. 4b, one recognizes that the peak width decreases and the peak height increases steadily with increasing  $Q_{max}$ : The peak form is largely determined by the truncation effect and the Fig. 4b gives, hence, an idea of the real space resolution of various techniques:  $Q_{max} = 14\text{\AA}^{-1}$  corresponds to a conventional x-ray diffraction experiment,  $Q_{max} = 23\text{\AA}^{-1}$  to the D4b neutron diffractometer of the ILL (Grenoble) and finally  $Q_{max} = 33\text{\AA}^{-1}$  can be easily reached with high energy photons. This behavior also proves, that the

region  $23\text{\AA}^{-1} < Q < 33\text{\AA}^{-1}$  still contains valuable information about this peak. The GeGe next neighbor distance in Fig. 4c, in contrary, does not change its form for  $Q_{max} > 23\text{\AA}^{-1}$ . The GeGe peak has consequently reached its natural form and extending the integration to higher Q values can only obscure the peak shape by inclusion of the high Q noise. From the position and the width of the GeO and the GeGe next neighbor peaks one can deduce the bond angle distribution.  $\alpha_0 = 133.0^\circ$  and  $\sigma = 8.3^\circ$ . This is in good agreement with an earlier x-ray structure determination [33] using Mo-K $\alpha$  x-rays (17.4 keV), ending with the more qualitative statement: "[...] *the average Ge-O-Ge angle is 133°. The distribution of Ge-O-Ge angles is fairly narrow but cannot be determined quantitatively with data of the present resolution.*"  $\chi$  defined by Eq. (8) is 2.0% in the range  $2.5\text{\AA} < r < 4.0\text{\AA}$  and 2.8% in the range from  $0 < r < 4\text{\AA}$ .  $\chi^2$  does not change significantly, when the  $\sigma_\delta$  parameter is changed from infinity (randomly distributed dihedral angles) to  $38^\circ$ . Decreasing  $\sigma_\delta$  further deteriorates the fit. In the limit of pure staggered or pure eclipsed conformation ( $\sigma_\delta \rightarrow 0$ ) a  $\chi$  of 6.5% and 5.9% is reached. The final model parameters are collected in Tab. 1. The model is compared to the experimental  $Qi(Q)$  in Fig. 5.

There is no indication for a sharp component in the bond angle distribution, which should be expected, if a significant volume fraction of the glass would reach crystalline order.

The question arises, whether the connection of the tetrahedral units is really that different in germania and silica. To answer this question a reanalysis of previous high energy photon experiments [1] was started, combining them with neutron diffraction data [2, 3] in the way described above. The most interesting of the first order differences  $d_{j'k'}$  presented above is the one where the OO contribution is removed. The Fourier-Bessel transform is shown in Fig. 6.  $Q_{max}$  has been chosen to be  $16\text{\AA}^{-1}$  for the reasons outlined in the previous section. The data are normalized according to Eq. 5 such that the SiSi partial structure factor has a constant weighting factor. Assuming again Si-O-Si bond angle distributions as in Eq. 10, broad distributions with  $\sigma > 10^\circ$  are clearly unacceptable. From that it follows that the assumption of isotropic dihedral angles is not justified. The geometric relations are such, that isotropic dihedral angles and narrow bond angle distributions lead to a shoulder or even a distinct peak on the low r side of the Si...O second neighbor peak. Some evidence was already collected by earlier authors on the non-randomness of the dihedral angles, but the literature is controversial in this point. So, e. g. Galeener [34] (from sterical arguments) and Evans *et al.* (from a comparison of various models with neutron diffraction data) suspected the dihedral angles to be non-randomly distributed. Gaskell *et al* [36] found a non uniform dihedral angle distribution in his relaxed version of the Bell and Dean [15] model, while Gladden [37] on the other hand found uniform dihedral angles in her models. The best agreement with the experiment is reached with  $\alpha_0 = 148.3^\circ$ ,  $\sigma = 7.5^\circ$  and  $\sigma_\delta = 27^\circ$ . The final parameters of the model are collected in Tab. 1

The interpretation of the NMR line-shape of silica glass is based on the knowledge of a relation between the chemical shift and the Si-O-Si angle. Four such relations are discussed in reference [17]: The secant [38], the linear [39], the point charge [40] and the s-hybridization [41] model. The secant and the s-hybridization model produce almost identical Si-O-Si angle distributions and are not considered separately. The resulting bond angle distributions are compared in Fig. 7 with each other, and with the distribution obtained in this work.  $\chi^2$  as a function of  $r_{max}$  is shown in Fig. 6. While the linear model gives a bad agreement with the combined neutron and photon data, the secant (with the data of Pettifer *et al.*) and point charge model give a comparable fit quality, but the lowest  $\chi$  of all NMR distributions has the bond angle distribution given by Gladden *et al.* These authors also used the secant

model to derive their bond angle distribution. It is interesting to note, that the tail to large angles present in many published Si-O-Si distributions is not necessary to explain the diffraction data. The  $\chi$  values reached by various distributions are reported in Tab. 2. All experimenters, of course, used different samples - with different concentrations of impurities and defects, different quenching conditions *etc.* - and this may also play a significant role at this level. It would be interesting to go an alternative route: The determination of the functional relation between chemical shift and bond angle by investigating the same glass sample with neutron and photon scattering and  $^{29}\text{Si}$ - MAS- NMR.

Several authors devoted special attention to the first sharp diffraction peak (FSDP) (see the discussion given by Elliot [42]). It is noted, that the FSDP vanishes almost completely when the SiO partial structure function is eliminated (Fig. 2). Probably the OO- and the SiSi- partial cancel as its weighting factors have different sign. Furthermore it is noted that the FSDP can not even be recognized any more if the contribution of the short range order is subtracted (Fig. 3). It is thus concluded that the FSDP by itself has very little structural significance as it is more or less arbitrarily composed of the weighted partial distribution functions and contributions of short and medium range order. This will be even worse in glasses of more complicated composition.

The experimental  $QS(Q)$  and  $Qi(Q)$  respectively are compared to the model in Fig. 8. The specified elements of the short and intermediate range order can describe both the neutron and photon diffraction pattern down to about  $2.5 \text{ \AA}^{-1}$ . The contribution of the different first and second neighbor distances to  $T_x(r)$  is shown in Fig. 9 and can be compared to Mozzi and Warrens Fig. 4 [10].

Finally, one should discuss what possibilities exist for a further disentangling of the partial structure factors. There is very little that can be done for silica. There are no suitable isotopes for oxygen, the scattering length difference between  $^{28}\text{Si}$  and  $^{29}\text{Si}$  is small (0.6fm) and  $^{29}\text{Si}$  is quite expensive. Anomalous diffraction and EXAFS spectroscopy are hindered by the low energy of the Si-K edge (1.8 keV). This is, why a combination of photon and neutron data is especially valuable in this case. In contrast, there are suitable Ge-isotopes for an isotope substitution experiment ( $^{70}\text{Ge}$  and  $^{73}\text{Ge}$ ) [26]. So,  $\text{GeO}_2$  could be a promising candidate to get a very detailed structural picture of a simple tetrahedral glass.

## 6 Conclusion

Combining neutron and photon diffraction can yield additional information on such well studied systems as the simple glasses. The ideal counterpart to modern neutron instrumentation are high energy photons in the energy range from  $\sim 80\text{-}200 \text{ keV}$ , which can be delivered from modern synchrotron radiation sources. The main advantages which come into play in the present study is the large accessible Q-range and the low absorption.

Due to the large accessible Q-range the GeGe next neighbor peak can be observed without any truncation effect. This leads to an accurate Ge-O-Ge bond angle distribution, the central parameter of a CRN description of the glass. There is no indication of a sharp component in the bond angle distribution, which could be expected, if a significant volume fraction of the glass would reach crystalline order.

Combining neutron and photon results can lead to an isolation of the SiSi first neighbor peak in  $\text{SiO}_2$ , too. From this, it can be deduced that the very broad Si-O-Si distribution calculated by Mozzi and Warren is not acceptable. This broad distribution is a consequence of the assumption of randomly distributed dihedral angles. Likewise the photon data used here would lead to a broad Si-O-Si bond angle distribution - when interpreted alone without



combination with neutron data and using this wrong assumption [1]. Only in combination with neutron data, it becomes clear that preference should be given to narrower distributions and the width of the Si-O-Si distribution is indeed within the experimental accuracy found to be identical to the width of the Ge-O-Ge angle distribution. From the bond angle distributions determined by  $^{29}\text{Si}$ -MAS-NMR the one given by Gladden *et al.* gave the best fit to the combined neutron and photon data. The Si-O-Si distributions determined from diffraction and from NMR measurements are in much better agreement, when neutron and photon diffraction are combined. Among the models relating the chemical shift to the bond angle the secant model agrees best with the diffraction data. These narrower distributions demand in turn a non-uniform distribution of the dihedral angles, that is to say a preference of the staggered conformation. The bond length, the Si-O-Si angle and the dihedral angle are likely to be correlated among each other and in neighboring units, but no evidence can be taken from diffraction experiments alone on these correlations.

## 7 Acknowledgments

Financial support of the Deutsche Forschungsgemeinschaft DFG under Grant No. Ne584/1-1 is gratefully appreciated.

## References

- [1] H. F. Poulsen, J. Neuefeind, H.-B. Neumann, J. R. Schneider and M. D. Zeidler, *J. Non-Cryst. Sol.* **188** (1995) 63
- [2] P. A. V. Johnson, A. C. Wright and R. N. Sinclair, *J. Non-Cryst. Sol.* **58** (1983) 109
- [3] D. I. Grimley, A. C. Wright and R. N. Sinclair, *J. Non-Cryst. Sol.* **119** (1990) 49
- [4] P. Debye and P. Scherrer, *Nachr. d. Königl. Ges. d. Wiss. z. Göttingen, Math.-phys. Klasse* (1916), 16; S. Kyropoulos, *Z. anorg. allg. Chem.* **99** (1917) 197
- [5] J. Tyndall, "Heat— A Mode of Motion.", London(1863); M. L. Frankenheim, "Die Lehre von der Cohäsion", Breslau (1835), 389
- [6] A. A. Lebedev, *Trudy Gos. Opt. Inst.* **2** (1921) 1
- [7] W. H. Zachariasen, *J. Am. Chem. Soc.* **54** (1932) 3841
- [8] A. C. Wright, PAC RIM Meeting, Honolulu, HI, USA, Nov. 1993, *J. Non-Cryst. Sol.* **179** (1994) 84
- [9] E. A. Porai-Koshits, *J. Non-Cryst. Sol.* **123** (1990) 1
- [10] R. L. Mozzi and B. E. Warren, *J. Appl. Crystallogr.* **2** (1969) 164
- [11] J. R. G. da Silva, D. G. Pinatti, C. E. Anderson and M. L. Rudee, *Philos. Mag.* **31** (1975) 713
- [12] P. G. Coombs, J. F. Natale, P. J. Hood, D. K. McElfresh, R. S. Wortman and J. F. Shackelford, *Phil. Mag.* **B51** (1985) L39
- [13] R. A. Barrio, F. L. Galeener, E. Martínez and R. J. Elliott, *Phys. Rev. B* **48** (1993) 15672

- [14] J. L. Robertson and S. C. Moss, *J. Non-Cryst. Sol.* **106** (1988) 330
- [15] R. J. Bell and P. Dean, *Phil. Mag.* **25** (1972) 1381
- [16] E. Dupree and R. F. Pettifer, *Nature* **308** (1984), 523
- [17] R. F. Pettifer, E. Dupree, I. Farnan and U. Sternberg, *J. Non-Cryst. Sol.* **106** (1988) 408
- [18] L. F. Gladden, T. A. Carpenter and S. R. Elliot, *Phil. Mag.* **53** (1986) L81
- [19] P. Vashishta, R. K. Kalia, J. P. Rino and I. Ebbsjö, *Phys. Rev. B* **41** (1990) 12197
- [20] B. Vessal, M. Armini and C. R. A. Catlow, *J. Non-Cryst. Sol.* **159** (1993) 184
- [21] B. P. Feuston and S. H. Garofalini, *J. Chem. Phys.* **89** (1988) 5818
- [22] J. Neuefeind, M. D. Zeidler and H. F. Poulsen, *Mol. Phys.* **87** (1996) 189
- [23] J. R. Schneider, *Synchr. Rad. News* **2**(8) (1995) 26
- [24] ESRF beam-line handbook Dec. 94, ed. R. Mason, p. 87; World Wide Web: <http://www.esrf.fr>
- [25] B. E. Warren, H. Krutter and O. Morningstar, *J. Am. Ceram. Soc.* **19** (1936) 202
- [26] L. Koester, H. Rauch and E. Seymann, *At. Data Nucl. Data Tabl.* **49** (1991) 65
- [27] J. H. Hubbell, W. J. Veigele, E. A. Briggs, R. T. Brown, D. T. Cromer and R. J. Howerton, *J. Phys. Chem. Ref. Data* **4** (1974) 471
- [28] J. H. Hubbell and I. Overbø, *J. Phys. Chem. Ref. Data* **8** (1979) 69
- [29] J. Waser and V. Schomaker, *Rev. Mod. Phys.* **25** (1953) 671
- [30] E. A. Lorch, *Phys. Rev. C* **2** (1969) 229
- [31] R. L. Mc Greevy and L. Puztai, *Molec. Simul.* **1** (1988) 359
- [32] D. A. Keen and R. L. McGreevy, *Nature* **344** (1990) 423
- [33] A. J. Leadbetter and A. C. Wright, *J. Non-Cryst. Sol.* **7** (1972) 37
- [34] F. L. Galeener *Phil. Mag. Letters* **B51** (1985) L1
- [35] K. M. Evans, P. H. Gaskell and C. M. M. Nex in 'The Structure of Non-Crystalline Materials, eds. P. H. Gaskell, J. M. Parker and E. A. Davis (1983), p. 426
- [36] P. H. Gaskell and I. D Tarrant, *Phil. Mag.* **B 42** (1980) 265
- [37] L. F. Gladden, *J. Non-Cryst. Sol.* **119** (1990) 318
- [38] J. V. Smith and C. S. Blackwell, *Nature* **303** (1983) 223
- [39] G. Engelhardt and R. Radeaglia, *Chem. Phys. Lett.* **108** (1984) 271
- [40] J. M. Thomas, J. Klinowski, S. Ramdas, B. K. Hunter and D. T. L. Tennakoon, *Chem. Phys. Lett.* **102** (1983) 158
- [41] U. Steinberg, *Mol. Phys.* **63** (1988) 249

[42] S. R. Elliot, *Nature* **354** (1991) 445

[43] R. N. Sinclair, D. A. G. Johnson, J. C. Dore, J. H. Clarke and A. C. Wright, *Nucl. Inst. Meth.* **117** (1974) 79

## 8 Figures

Figure 1: The fully corrected and normalized data (high energy photons, GeO<sub>2</sub>)

Full line: experimental intensity; dashed line: isotropic part of the scattering intensity (Self scattering + Compton scattering)

The insert is a zoom at the high-Q region.

Figure 2: The first order differences  $d_{j'k'}$  in amorphous silica

From top to bottom:  $Qd_{SiSi}(Q)$ ,  $Qd_{OO}(Q)$ ,  $Qd_{SiO}(Q)$ . Solid line: experimental  $Qd_{j'k'}(Q)$ , dashed line contribution of the first two peaks (SiO-, OO-) in real space.

Figure 3: The first order differences in amorphous silica, contributions of the first two peaks in real space removed

From top to bottom:  $Qd_{SiSi}(Q)$ ,  $Qd_{OO}(Q)$ ,  $Qd_{SiO}(Q)$ .

Figure 4:  $T_x(r)$  for vitreous germania

a)  $T_x(r)$  for vitreous germania,  $Q_{max} = 23\text{\AA}^{-1}$

b) and c) Closer look at the GeO- and the GeGe-peak respectively: solid line  $Q_{max} = 33\text{\AA}^{-1}$ , dashed line  $Q_{max} = 23\text{\AA}^{-1}$ , dots  $Q_{max} = 14\text{\AA}^{-1}$

Figure 5: Comparison of the model distribution for GeO<sub>2</sub> with experiment

Solid line: experimental  $Qi(Q)$ , dashed line: model  $Qi(Q)$

Figure 6:  $T_{OO}(r)$  and  $\chi^2$  from the various distributions

Upper window:  $T_{OO}(r)$ ; lower window  $\chi^2$  ( $\chi^2$  is not normalized to  $\int T_{exp}^2(r)$  here).

Full line: experiment, dashed triple dotted: Mozzi and Warrens distribution [10], 1. dotted line: Best fit of Eq. (10), 2. dashed dotted line: NMR model of ref. [18], 3-5: NMR models discussed in ref. [17]; 3. linear model (not shown) 4. dashed double dotted line: NMR data of ref. [17], point charge model; 5. dashed line NMR data of ref. [17], secant model; 6. triple dotted line: best fit of Eq. (10) to the NMR distribution of ref. [18]

Figure 7: Various models for the Si-O-Si bond angle

1. dotted line: Best fit of Eq. (10) to the combined photon and neutron data, 2. dashed dotted line: NMR result from ref. [18], based on the secant model; 3-5: NMR models discussed in ref. [17]; 3. dashed triple dotted line: linear model, 4. dashed double dotted line: point charge model, 5. dashed line: secant model. 6. triple dotted line: best fit of Eq. (10) to the NMR result from ref. [18]

Figure 8: Comparison of the model for SiO<sub>2</sub> with the experiment

Solid line: experimental  $QS(Q)$  and  $Qi(Q)$  respectively; dashed line: model  $QS(Q)$  and  $Qi(Q)$  respectively. a) photon diffraction [1], b) neutron diffraction [2, 3]

The neutron data were available as spline fit to the experimental data only.

Figure 9: First and second shell contributions to  $T_x(r)$

Solid line: experimental  $T_x(r)$  and Fourier transform of the residue with  $Q_{max} = 10.6\text{\AA}^{-1}$ , dashed line: SiO- and OO- first neighbor, dotted line: SiSi- first shell, dashed dotted: SiO- second shell, triple dotted line: OO second shell, double dotted line SiSi- second shell contribution

Table 1: Structural parameters for SiO<sub>2</sub> and GeO<sub>2</sub>

	$r_{AX}$	$\sigma_r$	$\alpha_0$	$\sigma_\alpha$	$\beta_0$	$\sigma_\beta$	$\sigma_\delta$
GeO <sub>2</sub>	1.73	.0415	133.0	8.3	109.47 <sup>1</sup>	4.2 <sup>2</sup>	38
SiO <sub>2</sub>	1.605 <sup>3</sup>	.0493 <sup>3</sup>	148.3	7.5	109.47 <sup>1</sup>	4.2 <sup>3</sup>	27

Distances in Å, angles in degree.

1: Not refined,  $\beta_0$  is taken from the ideal tetrahedron

2: Not refined, taken to be equal to SiO<sub>2</sub>

3: Not refined, taken from reference [3]

Table 2:  $\chi$  reached from various bond angle models

This work		0.84%
Gladden <i>et al.</i> [18]		1.4%
Pettifer <i>et al.</i> [17]	secant model	2.26%
	point charge model	2.20%
	linear model	3.41%

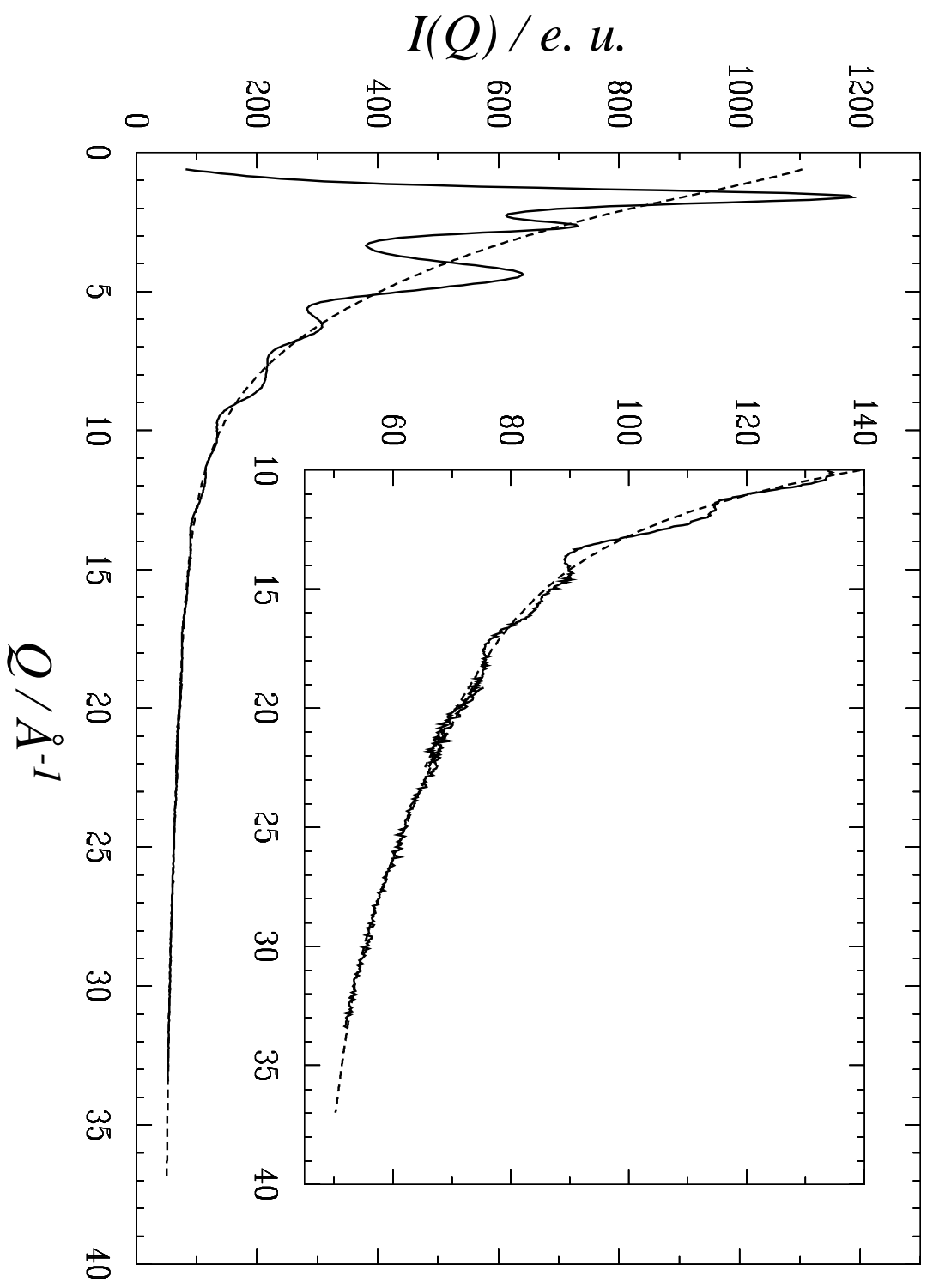
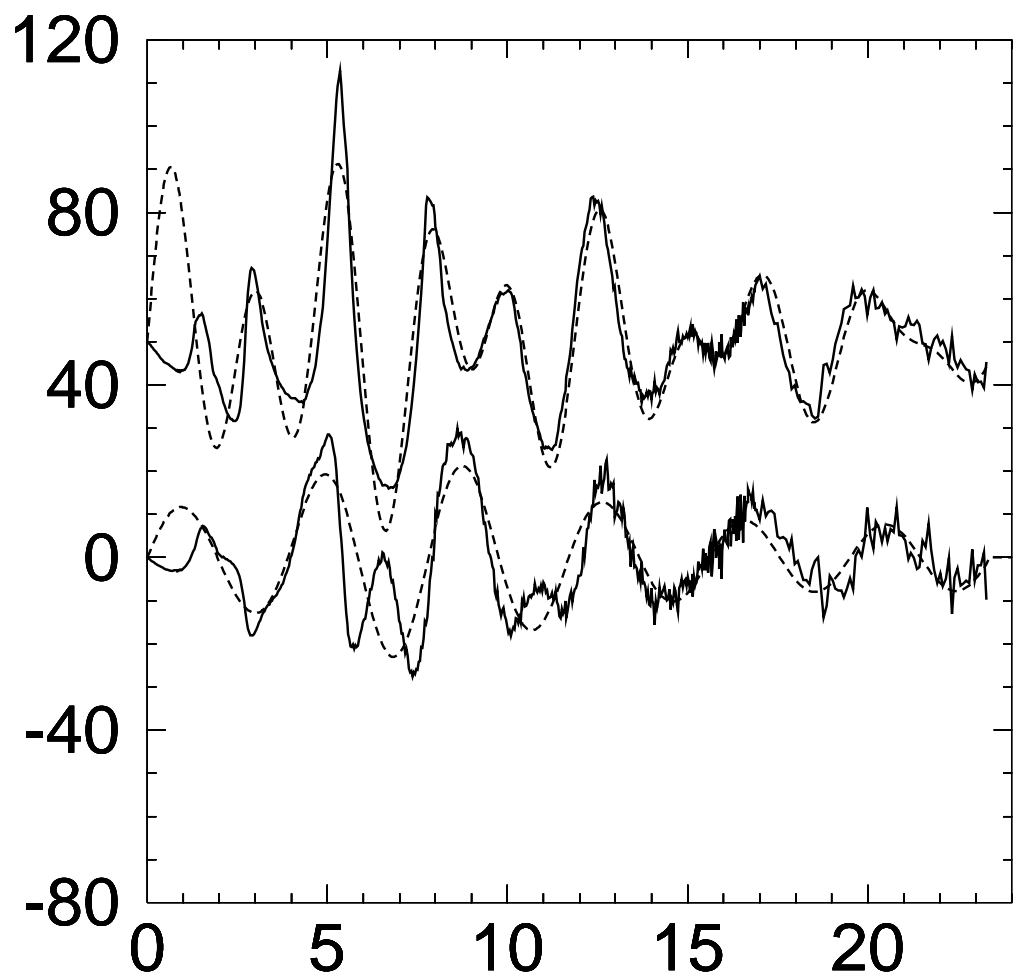
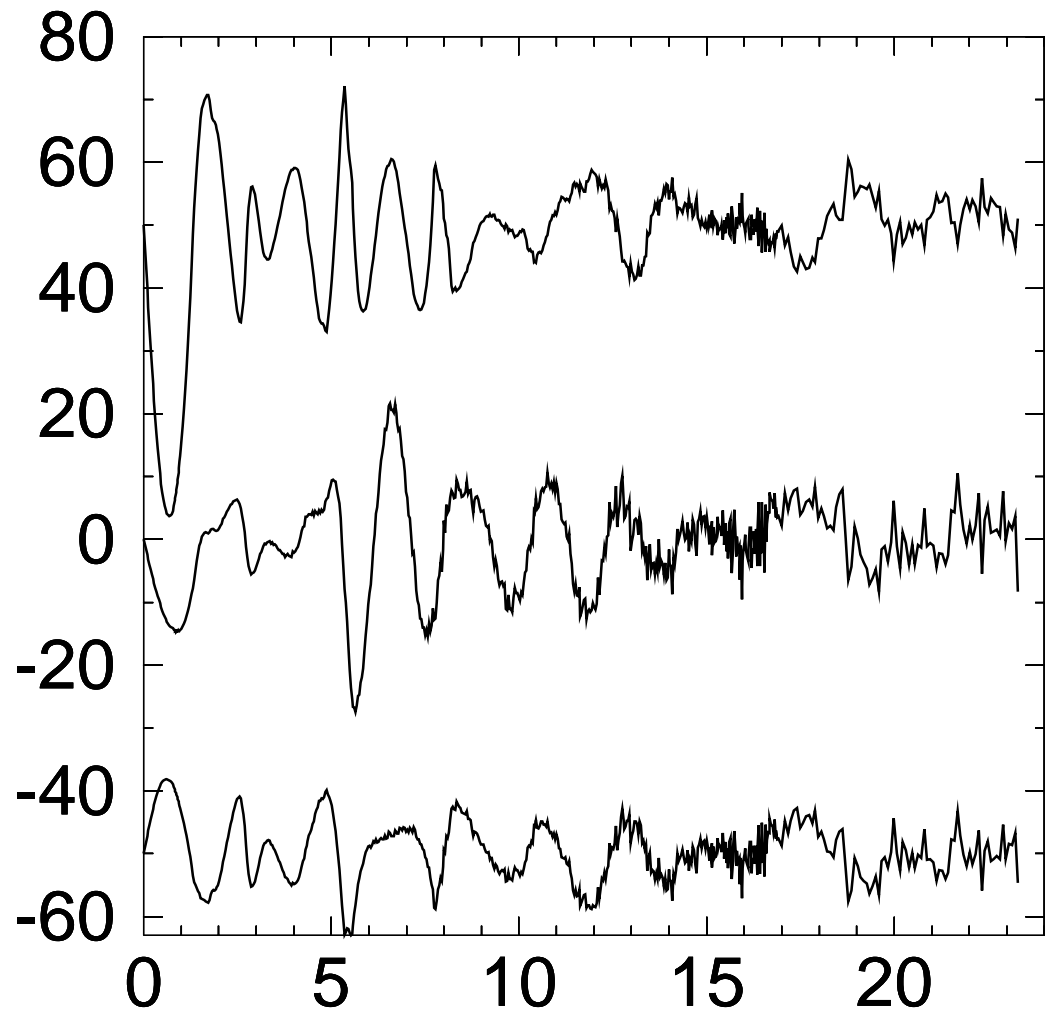
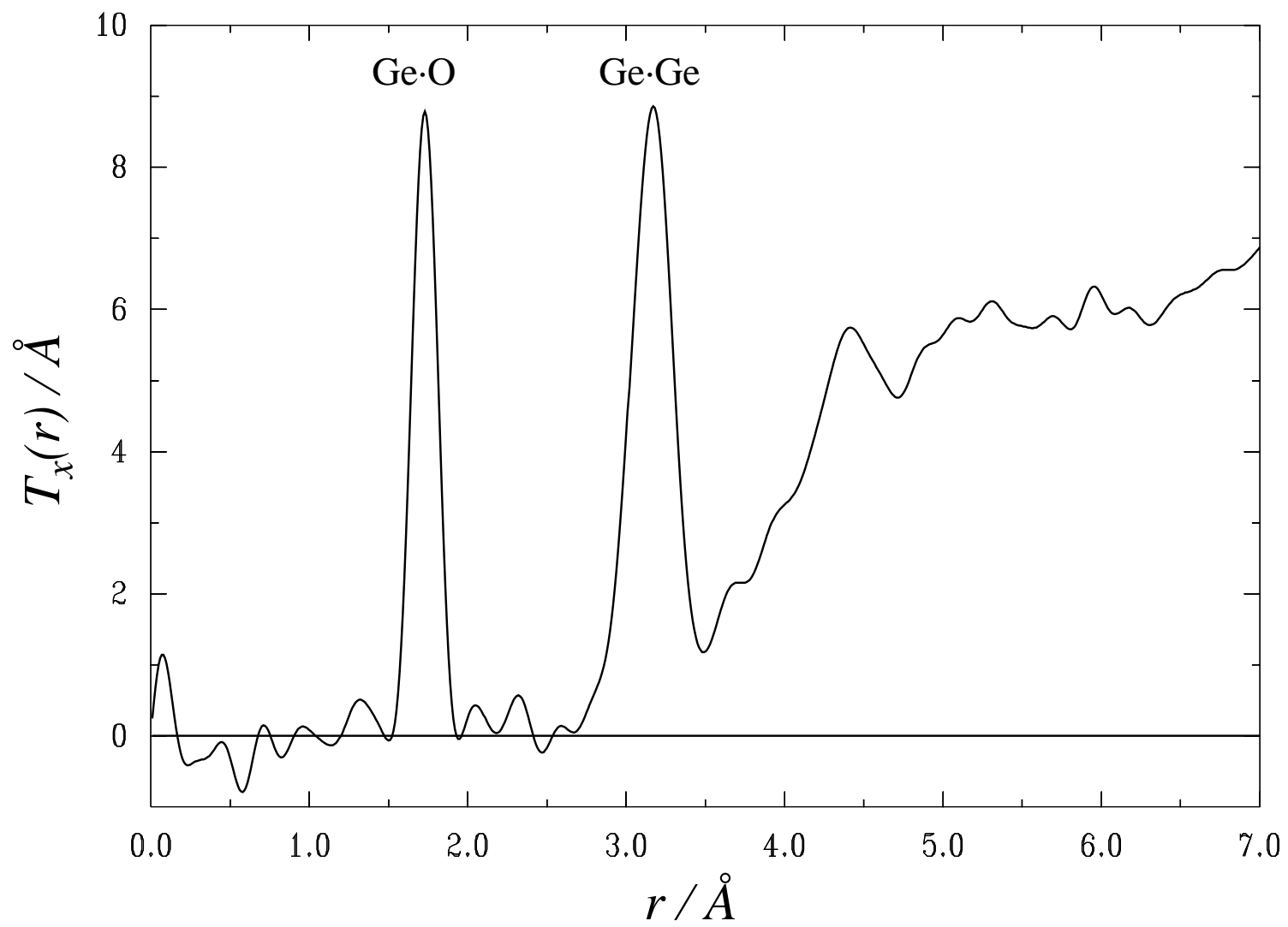


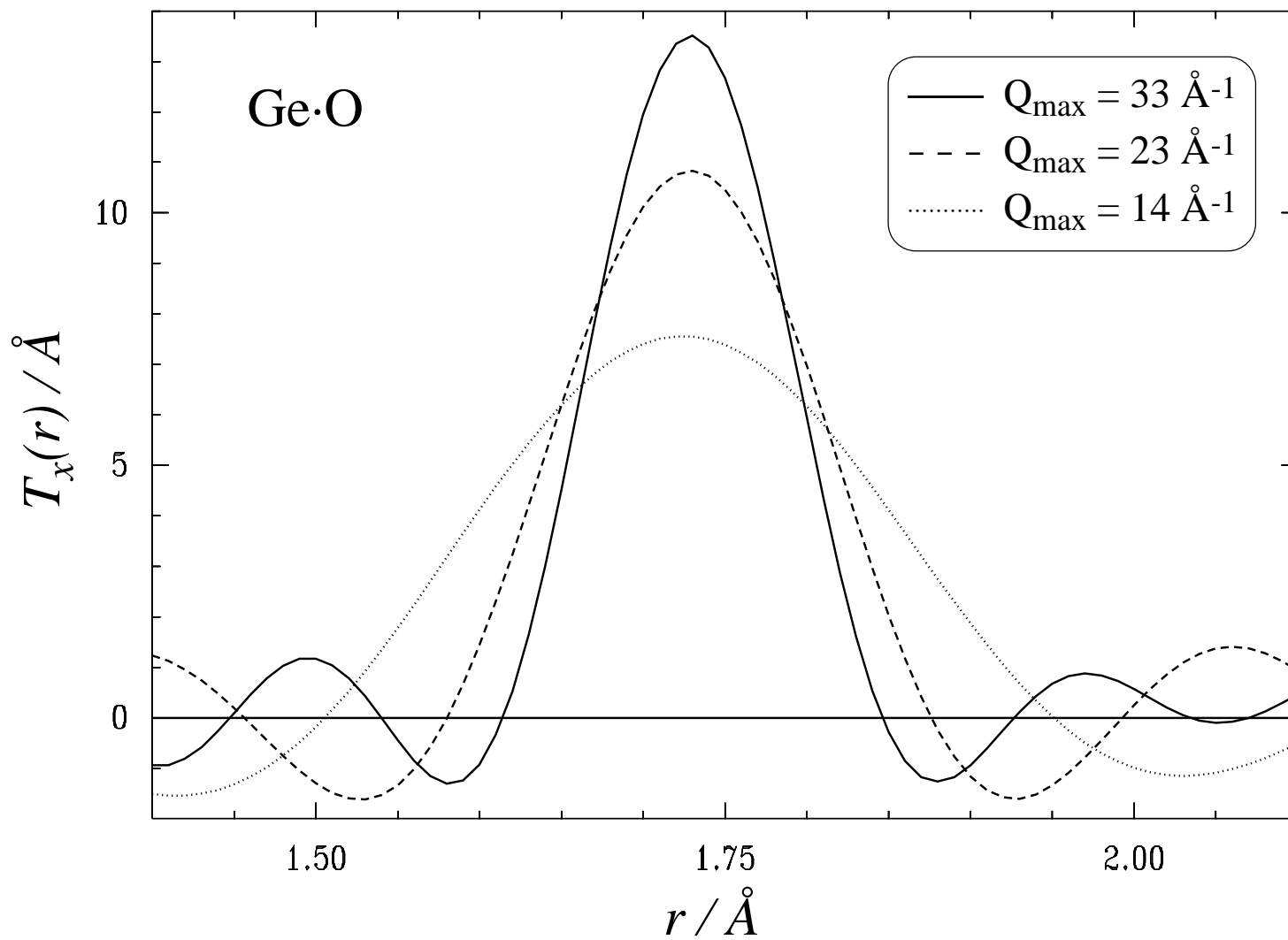
Figure 1











Figure

